Two-color resonant four-wave mixing: Analytical expressions for signal intensity

Skip Williams,[a] Eric A. Rohlfing,[b] and Larry A. Rahn
Combustion Research Facility, Sandia National Laboratories, Livermore, California 94551

Richard N. Zare[b]
Department of Chemistry, Stanford University, Stanford, California 94305

(Received 16 September 1996; accepted 13 November 1996)

We present analytical signal expressions for each two-color resonant four-wave mixing (TC-RFWM) scheme that can be used for double-resonance molecular spectroscopy in the limit of weak fields (no saturation). The theoretical approach employs time-independent, diagrammatic perturbation theory and a spherical tensor analysis in an extension of recent treatments of degenerate four-wave mixing [S. Williams, R. N. Zare, and L. A. Rahn, J. Chem. Phys. **101**, 1072 (1994)] and TC-RFWM for the specific case of stimulated emission pumping [S. Williams *et al.*, J. Chem. Phys. **102**, 8342 (1995)]. Under the assumption that the relaxation of the population, the orientation, and the alignment are the same, simple analytic expressions are derived for commonly used experimental configurations. The TC-RFWM signal is found to be a product of a concentration term, a one-photon molecular term, a line shape function, and a laboratory-frame geometric factor. These expressions are intended to facilitate the practical analysis of TC-RFWM spectra by clarifying, for example, the dependence on beam polarizations and rotational branch combinations. © *1997 American Institute of Physics.* [S0021-9606(97)01307-X]

I. INTRODUCTION

Resonant four-wave mixing (RFWM) describes a broad class of nonlinear optical techniques that have been applied in the spectroscopy and remote sensing of stable and transient molecules in a variety of gas-phase environments. Degenerate four-wave mixing (DFWM), in which all of the fields are of a single frequency, has been used as a diagnostic in combustion[1–6] and reacting plasmas.[7–9] In addition, DFWM in the phase conjugate phase matching geometry has long been recognized as a technique for high-resolution (sub-Doppler) spectroscopy[10] and has recently been demonstrated as a method of detecting transitions in stimulated emission pumping (SEP) spectroscopy.[11,12] Two-color resonant four-wave mixing (TC-RFWM) describes another set of fully resonant wave mixing processes in which two optical fields have frequencies in resonance with two distinct molecular transitions. Because of its coherent, background-free nature, TC-RFWM has potential as a tool for various double-resonance schemes in molecular spectroscopy (here we use ''double resonance'' in the spectroscopic sense where two transitions share a common level). TC-RFWM has recently been used to perform excited-state double-resonance spectroscopy on stable molecules[13,14] and to provide background-free SEP spectra of stable[15] and transient species.[16,17] Very recently, TC-RFWM was used to detect the CH radical in an oxyacetylene flame.[18]

Signal generation in RFWM can be interpreted as the formation of and diffraction from laser-induced gratings.[19] The conceptually appealing grating picture is particularly applicable to TC-RFWM in which there is a distinct difference in frequency (and possibly temporal delay) between the two grating forming beams and the probe beam. Thus TC-RFWM techniques have also become known as two-color laser-induced grating spectroscopy (TC-LIGS).[13,14,20–24] We have recently sought to describe RFWM in a formalism more amenable to the interpretation of molecular spectra than the laser-induced grating picture. Our approach, which we have applied both to DFWM[25] and to the specific case of SEP using TC-RFWM,[17] combines time-independent diagrammatic perturbation theory[26–29] with a spherical tensor analysis[30] to derive analytical signal expressions for the RFWM signal in a manner that accounts for polarization, collisional, and velocity effects in the weak-field (nonsaturating) limit. This approach is particularly powerful, because it separates the factors that depend on the interaction of the molecule with the fields in the molecular frame from those factors relating to the interaction of the molecule with the fields in the laboratory frame.

In this paper, we generalize our previous theoretical treatment for the two TC-RFWM processes appropriate to SEP[17] to include all possible schemes by which TC-RFWM can be used for double-resonance molecular spectroscopy. The final results are weak-field signal expressions for one-photon resonant TC-RFWM processes that should provide experimentalists with the necessary tools to interpret geometric (polarization) and relaxation (line shapes) effects in TC-RFWM. We consider three input fields of arbitrary polarization that interact with an isotropic sample to produce a fourth field and assume that field propagation effects can be ignored (negligible absorption). We assume that the TC-RFWM process couples levels of sharp (definite) angular momentum **J** (omitting nuclear spin) and, therefore, our results may be

[a]Permanent address: Phillips Laboratory/GPID, 29 Randolph Rd. Hanscom, AFB, MA 01731.
[b]Authors to whom all correspondence should be addressed.

 0021-9606/97/106(8)/3090/13/$10.00

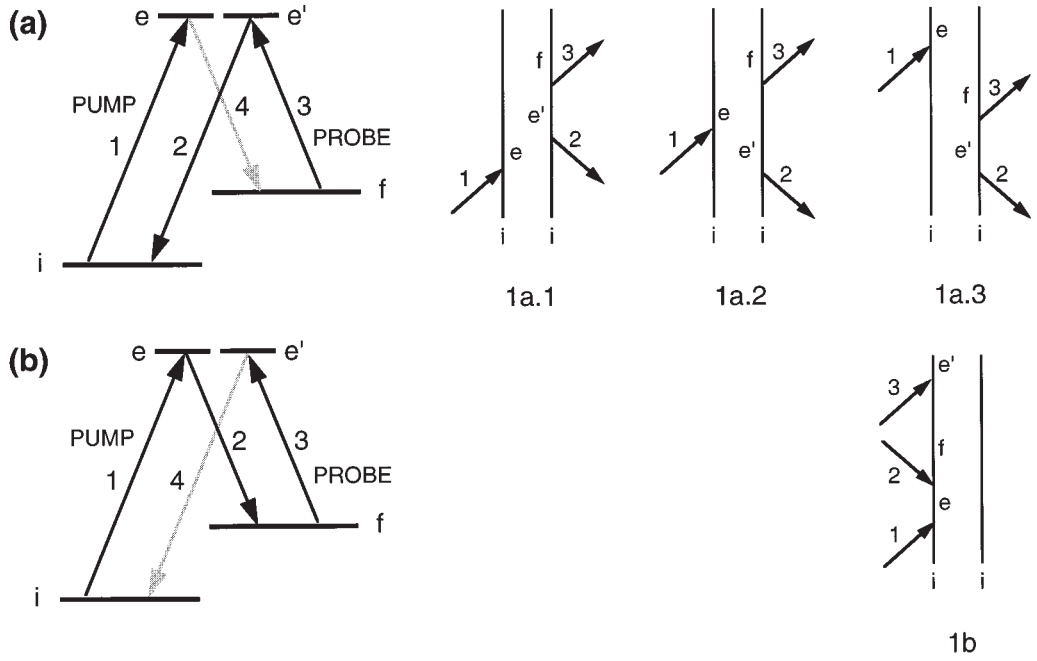

FIG. 1. Folded energy-level schematics and double-sided Feynman diagrams used to identify the resonant terms in $\chi^{(3)}$ for the TC-RFWM schemes appropriate to SEP spectroscopy: (a) $\omega_1=\omega_2$ (PUMP) and $\omega_3=\omega_4$ (PROBE or DUMP); (b) $\omega_1=\omega_4$ (PUMP) and $\omega_3=\omega_2$ (PROBE or DUMP). The letter labels refer to specific degenerate magnetic sublevels in each rovibronic state; the letters e and e' denote magnetic sublevels (either the same or different) in the excited state.

used quite generally for all molecules for which J is a good quantum number. The four-photon matrix elements that account for polarization effects have been previously evaluated for resonant coherent anti-Stokes Raman spectroscopy (CARS)[31] and RFWM[32] in several Hund's coupling cases for diatomic molecules. However, these results are basis-set dependent and therefore not as readily generalized to other systems, i.e., asymmetric tops. Our theoretical approach[25] is universal in that it may be generalized to include noncollinear phase matching geometries, arbitrary field polarizations, and cases where the molecular population, orientation, and alignment relax at different rates. In this paper, however, we focus on the specific, but common, case of linearly polarized fields that interact in nearly collinear phase matching geometries in environments where the multipole moments of the total angular momentum distribution (the population, the orientation, and the alignment) relax independently (isotropic relaxation) and at the same rate.

The remainder of this paper is organized into three sections. In Sec. II we present the TC-RFWM schemes and develop signal expressions for TC-RFWM as a function of input field polarization, rotational branch, collisional relaxation and dephasing, and molecular velocity. This section outlines the key steps involved in the derivation and is intended as a guide for the experimentalist. The details of the method are given elsewhere.[17,25] In Sec. III we discuss some additional issues to be considered before applying the expressions of Sec. II. We summarize our findings in Sec. IV.

II. TC-RFWM PROCESSES AND SIGNAL EXPRESSIONS

A. TC-RFWM schemes

In Figs. 1–3 we present the three-level energy diagrams and field labelings for each possible application of TC-RFWM to double-resonance spectroscopy. The level labels correspond to individual magnetic sublevels, either the same or different, of each rovibronic state where i denotes levels in the ground state and e and f denote levels in excited states. RFWM is subject to both energy and phase matching constraints. In TC-RFWM there are three types of spectroscopic schemes that can be constructed within the energy constraints of two resonant input frequencies. Figures 1 and 2 each illustrate double resonances where the excited-state level e is common to both transitions. The folded diagram in Fig. 1 corresponds to SEP spectroscopy in which the $e-i$ transition is the PUMP and the $e-f$ transition is (for consistency) denoted as the PROBE. The probe transition is more commonly referred to as the DUMP transition in SEP. Figure 2 shows the unfolded diagram appropriate to excited-state spectroscopy (often called optical–optical double resonance or OODR) in which the $e-i$ transition is the again the PUMP and the $f-e$ transition is the PROBE. For each of these excited-state common schemes, there are two possible RFWM energy level diagrams that satisfy the same energy conservation constraints but have different phase matching criteria, i.e., (a) $\omega_1=\omega_2$ (PUMP) and $\omega_3=\omega_4$ (PROBE) and (b) $\omega_1=\omega_4$ (PUMP) and $\omega_3=\omega_2$ (PROBE). Figure 3 illus-

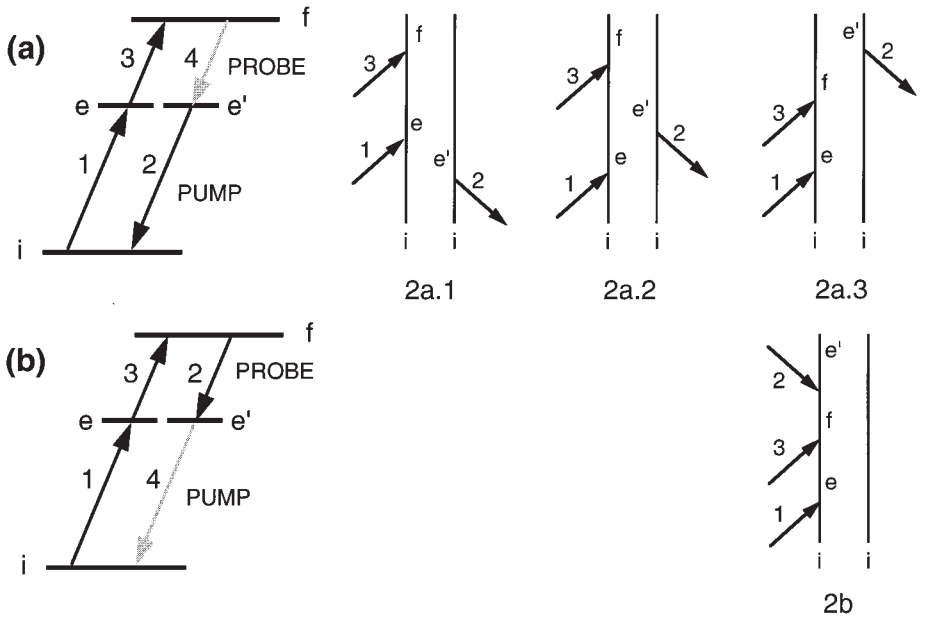

FIG. 2. Unfolded energy-level schematics and double-sided Feynman diagrams used to identify the resonant terms in $\chi^{(3)}$ for the TC-RFWM schemes appropriate to excited-state PUMP/PROBE spectroscopy: (a) $\omega_1=\omega_2$ (PUMP) and $\omega_3=\omega_4$ (PROBE); (b) $\omega_1=\omega_4$ (PUMP) and $\omega_3=\omega_2$ (PROBE). The letter labels refer to specific degenerate magnetic sublevels in each rovibronic state; the letters e and e' denote magnetic sublevels (either the same or different) in the excited state.

trates a double resonance in which the ground-state level i is the common level. Here the $e-i$ transition is the PUMP and the $f-i$ transition is the PROBE. This double-resonance approach is often referred to as hole-burning spectroscopy since the effect of the PUMP laser is to burn a hole in the ground state population that is detected by its effect on the action (usually fluorescence) induced by the PROBE laser. There is only one TC-RFWM energy level diagram for hole-burning spectroscopy, because both transitions sample the initially populated level and their labeling as PUMP and PROBE is arbitrary.

B. General expressions for $\chi^{(3)}$

In four-wave mixing, three incoming waves with electric fields $\mathbf{E}_1(\mathbf{r},t)$, $\mathbf{E}_2(\mathbf{r},t)$, and $\mathbf{E}_3(\mathbf{r},t)$, propagation vectors $\mathbf{k}_1$, $\mathbf{k}_2$, and $\mathbf{k}_3$, and frequencies ω_1, ω_2, and ω_3 interact through the third-order nonlinear susceptibility $\chi^{(3)}$ to generate a fourth field, $\mathbf{E}_4$, with propagation vector $\mathbf{k}_4$ and frequency ω_4. The electric fields are defined as

$$\mathbf{E}_j(\mathbf{r},t)=\tfrac{1}{2}\mathbf{E}_j e^{-i(\omega_j t-\mathbf{k}_j\cdot\mathbf{r})}+\text{c.c.}, \quad \mathbf{E}_j=E_j\boldsymbol{\epsilon}_j, \tag{1}$$

where $\mathbf{E}_j$ is the vector amplitude, E_j is the scalar amplitude, and $\boldsymbol{\epsilon}_j$ is the normalized $(\boldsymbol{\epsilon}_j\cdot\boldsymbol{\epsilon}_j^*=1)$ polarization unit vector of the electric field labeled j. The conventions for expressing the unit vectors are given in the appendix of Ref. 25. The intensity of each electric field $\mathbf{E}_j(\mathbf{r},t)$ is given by

$$I_j=\epsilon_0 c\langle|\mathbf{E}_j(\mathbf{r},t)|^2\rangle=\frac{\epsilon_0 c}{2}|E_j|^2, \tag{2}$$

where the angular brackets denote a cycle average and j is the field label, ϵ_0 is the permittivity of free space, and c is the speed of light. The result of the interaction of the three elec-

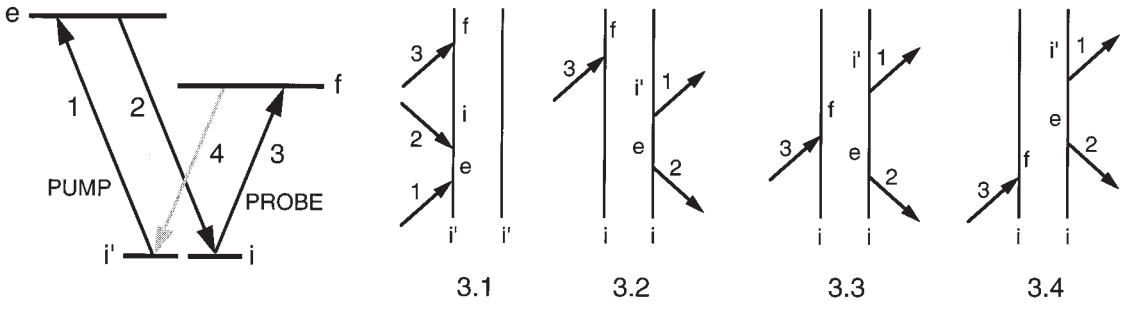

FIG. 3. Open energy-level schematics and double-sided Feynman diagrams used to identify the resonant terms in $\chi^{(3)}$ for the TC-RFWM process appropriate to ground-state double-resonance (hole-burning) spectroscopy: $\omega_1=\omega_2$ (PUMP) and $\omega_3=\omega_4$ (PROBE). The letter labels refer to specific degenerate magnetic sublevels in each rovibronic state; the letters i and i' denote magnetic sublevels (either the same or different) in the ground state.

tric fields with the molecular sample is the generation of the third-order electric polarization $\mathbf{P}^{(3)}(\mathbf{r},t)$. We note that many conventions exist for expressing $\mathbf{P}^{(3)}(\mathbf{r},t)$. Therefore, for clarity, we follow the convention of Butcher and Cotter[33] throughout and write $\mathbf{P}^{(3)}(\mathbf{r},t)$ in SI units as

$$\mathbf{P}^{(3)}(\mathbf{r},t)=\tfrac{1}{2}\mathbf{P}^{(3)}_{\mathrm{RFWM}}e^{-i(\omega_4 t-\mathbf{k}_4\cdot\mathbf{r})}+\mathrm{c.c.},$$

$$\mathbf{P}^{(3)}_{\mathrm{RFWM}}=\wp^{(3)}_{\mathrm{RFWM}}\boldsymbol{\epsilon}_4, \tag{3}$$

where $\mathbf{P}^{(3)}_{\mathrm{RFWM}}$ is the vector amplitude, $\wp^{(3)}_{\mathrm{RFWM}}$ is the scalar amplitude, and $\boldsymbol{\epsilon}_4$ is the normalized ($\boldsymbol{\epsilon}_j\cdot\boldsymbol{\epsilon}_j^*=1$) polarization unit vector.

The RFWM signal intensity is proportional to the cycle average of the absolute square of the third-order nonlinear polarization. In analogy with Eq. (2), the RFWM signal intensity is proportional to the absolute value squared of the scalar amplitude $\wp^{(3)}_{\mathrm{RFWM}}$,

$$I_{\mathrm{RFWM}}=I_4\propto\langle|\mathbf{P}^{(3)}(\mathbf{r},t)|^2\rangle=\tfrac{1}{2}|\wp^{(3)}_{\mathrm{RFWM}}|^2. \tag{4}$$

Therefore our concern is to calculate $\wp^{(3)}_{\mathrm{RFWM}}$ for two-color schemes with $\omega_1\neq\omega_3$ where

$$\wp^{(3)}_{\mathrm{TC\text{-}RFWM}}=\mathbf{P}^{(3)}_{\mathrm{TC\text{-}RFWM}}\cdot\boldsymbol{\epsilon}_4^*$$
$$=\epsilon_0\tfrac{3}{2}\boldsymbol{\chi}^{(3)}_{\mathrm{TC\text{-}RFWM}}(-\omega_4,\omega_1,\omega_3,-\omega_2)E_1E_2^*E_3 \tag{5}$$

and $\chi^{(3)}_{\mathrm{TC\text{-}RFWM}}(-\omega_4,\omega_1,\omega_3,-\omega_2)$ is the scalar form of the third-order susceptibility. (See Ref. 33, pp. 24–28.)

The general expression for $\boldsymbol{\chi}^{(3)}$ that applies here consists of 48 terms that completely describe the interaction of the electric fields with the molecular system.[26–28] These terms differ in the time ordering of the interaction fields and the permutations of the quantum states involved. Evaluating all of these terms is a formidable task in general; however, in a fully resonant four-wave mixing experiment, the intensity at a particular resonance in the spectrum is dominated by only a few terms.[26,31] We assume that the excitation bandwidth is sufficiently narrow compared with the density of states (including Doppler broadening) of the absorbing molecules so that the interaction is exclusively between the levels involved in the one-photon resonant transitions. Furthermore, we consider the case where the rovibronic state i is initially populated, and the e and f rovibronic states are initially unpopulated ($N_{e,f}/N_i<10^{-2}$). The summation over all state permutations then reduces to a summation over the magnetic sublevels of the initial rovibronic state. Because the initial magnetic sublevel distribution is assumed to be isotropic, i.e., all degenerate M sublevels are equally populated and no phase relation exists between them, the summation is equally weighted.

The significant contributions to the third-order nonlinear susceptibility for each TC-RFWM scheme may be written down directly from the double-sided Feynman diagrams presented in Figs. 1–3. The double-sided Feynman diagrams of Fig. 1(a) represent the following expression for $\chi^{(3)}_{1a}(-\omega_4,\omega_1,\omega_3,-\omega_2)$ in the perturbative (weak-field) limit:

$$\chi^{(3)}_{1a}(-\omega_4,\omega_1,\omega_3,-\omega_2)=\frac{N}{6\epsilon_0\hbar^3}\left\{\sum_{all\ M}\frac{\rho^{(0)}_{ii}\langle e|\boldsymbol{\epsilon}_1\cdot\boldsymbol{\mu}|i\rangle\langle i|\boldsymbol{\epsilon}_2^*\cdot\boldsymbol{\mu}|e'\rangle\langle e'|\boldsymbol{\epsilon}_3\cdot\boldsymbol{\mu}|f\rangle\langle f|\boldsymbol{\epsilon}_4^*\cdot\boldsymbol{\mu}|e\rangle}{(\omega_{ei}-\omega_1+\mathbf{k}_1\cdot\mathbf{v}-i\Gamma_{ei})[(\mathbf{k}_1-\mathbf{k}_2)\cdot\mathbf{v}-i\Gamma_{ee'}](\omega_{ef}-\omega_4+\mathbf{k}_4\cdot\mathbf{v}-i\Gamma_{ef})}\right.$$
$$-\sum_{all\ M}\frac{\rho^{(0)}_{ii}\langle e|\boldsymbol{\epsilon}_1\cdot\boldsymbol{\mu}|i\rangle\langle i|\boldsymbol{\epsilon}_2^*\cdot\boldsymbol{\mu}|e'\rangle\langle e'|\boldsymbol{\epsilon}_3\cdot\boldsymbol{\mu}|f\rangle\langle f|\boldsymbol{\epsilon}_4^*\cdot\boldsymbol{\mu}|e\rangle}{(\omega_{e'i}-\omega_2+\mathbf{k}_2\cdot\mathbf{v}+i\Gamma_{e'i})[(\mathbf{k}_1-\mathbf{k}_2)\cdot\mathbf{v}-i\Gamma_{ee'}](\omega_{ef}-\omega_4+\mathbf{k}_4\cdot\mathbf{v}-i\Gamma_{ef})}$$
$$\left.+\sum_{all\ M}\frac{\rho^{(0)}_{ii}\langle f|\boldsymbol{\epsilon}_4^*\cdot\boldsymbol{\mu}|e\rangle\langle e|\boldsymbol{\epsilon}_1\cdot\boldsymbol{\mu}|i\rangle\langle i|\boldsymbol{\epsilon}_2^*\cdot\boldsymbol{\mu}|e'\rangle\langle e'|\boldsymbol{\epsilon}_3\cdot\boldsymbol{\mu}|f\rangle}{(\omega_{e'i}-\omega_2+\mathbf{k}_2\cdot\mathbf{v}+i\Gamma_{e'i})[-\omega_{fi}-\omega_3+\omega_2+(\mathbf{k}_3-\mathbf{k}_2)\cdot\mathbf{v}-i\Gamma_{fi}](\omega_{ef}-\omega_4+\mathbf{k}_4\cdot\mathbf{v}-i\Gamma_{ef})}\right\}. \tag{6}$$

The three terms in Eq. (6) correspond to the diagrams labeled 1a.1–1a.3 in Fig. 1, respectively, and correspond to the three possible fully resonant time orderings of the three input fields. The significant contribution to the TC-RFWM third-order nonlinear susceptibility for scheme 1b is represented using a single double-sided Feynman diagram in Fig. 1(b). The resulting expression is

$$\chi^{(3)}_{1b}(-\omega_4,\omega_1,\omega_3,-\omega_2)$$
$$=\frac{N}{6\epsilon_0\hbar^3}\sum_{all\ M}\frac{\rho^{(0)}_{ii}\langle i|\boldsymbol{\epsilon}_4^*\cdot\boldsymbol{\mu}|e'\rangle\langle e'|\boldsymbol{\epsilon}_3\cdot\boldsymbol{\mu}|f\rangle\langle f|\boldsymbol{\epsilon}_2^*\cdot\boldsymbol{\mu}|e\rangle\langle e|\boldsymbol{\epsilon}_1\cdot\boldsymbol{\mu}|i\rangle}{(\omega_{ei}-\omega_1+\mathbf{k}_1\cdot\mathbf{v}-i\Gamma_{ei})[\omega_{fi}-\omega_1+\omega_2+(\mathbf{k}_1-\mathbf{k}_2)\cdot\mathbf{v}-i\Gamma_{fi}](\omega_{e'i}-\omega_4+\mathbf{k}_4\cdot\mathbf{v}-i\Gamma_{e'i})}. \tag{7}$$

Continuing in a similar fashion, the three double-sided Feynman diagrams labeled 2a.1–2a.3 represent the following expression for the nonlinear susceptibility for scheme 2a:

$$\chi^{(3)}_{2a}(-\omega_4,\omega_1,\omega_3,-\omega_2)=\frac{N}{6\epsilon_0\hbar^3}\left\{\sum_{all\ M}\frac{\rho^{(0)}_{ii}\langle e'|\boldsymbol{\epsilon}^*_4\cdot\boldsymbol{\mu}|f\rangle\langle f|\boldsymbol{\epsilon}_3\cdot\boldsymbol{\mu}|e\rangle\langle e|\boldsymbol{\epsilon}_1\cdot\boldsymbol{\mu}|i\rangle\langle i|\boldsymbol{\epsilon}^*_2\cdot\boldsymbol{\mu}|e'\rangle}{(\omega_{e'i}-\omega_2+\mathbf{k}_2\cdot\mathbf{v}+i\Gamma_{e'i})[(\mathbf{k}_1-\mathbf{k}_2)\cdot\mathbf{v}-i\Gamma_{ee'}](\omega_{fe'}-\omega_4+\mathbf{k}_4\cdot\mathbf{v}-i\Gamma_{fe'})}\right.$$
$$-\sum_{all\ M}\frac{\rho^{(0)}_{ii}\langle e'|\boldsymbol{\epsilon}^*_4\cdot\boldsymbol{\mu}|f\rangle\langle f|\boldsymbol{\epsilon}_3\cdot\boldsymbol{\mu}|e\rangle\langle e|\boldsymbol{\epsilon}_1\cdot\boldsymbol{\mu}|i\rangle\langle i|\boldsymbol{\epsilon}^*_2\cdot\boldsymbol{\mu}|e'\rangle}{(\omega_{ei}-\omega_1+\mathbf{k}_1\cdot\mathbf{v}-i\Gamma_{et})[(\mathbf{k}_1-\mathbf{k}_2)\cdot\mathbf{v}-i\Gamma_{ee'}](\omega_{fe'}-\omega_4+\mathbf{k}_4\cdot\mathbf{v}-i\Gamma_{fe'})}$$
$$\left.-\sum_{all\ M}\frac{\rho^{(0)}_{ii}\langle f|\boldsymbol{\epsilon}_3\cdot\boldsymbol{\mu}|e\rangle\langle e|\boldsymbol{\epsilon}_1\cdot\boldsymbol{\mu}|i\rangle\langle i|\boldsymbol{\epsilon}^*_2\cdot\boldsymbol{\mu}|e'\rangle\langle e'|\boldsymbol{\epsilon}^*_4\cdot\boldsymbol{\mu}|f\rangle}{(\omega_{ei}-\omega_1+\mathbf{k}_1\cdot\mathbf{v}-i\Gamma_{et})[\omega_{fi}-\omega_1-\omega_3+(\mathbf{k}_1+\mathbf{k}_3)\cdot\mathbf{v}-i\Gamma_{fi}](\omega_{fe'}-\omega_4+\mathbf{k}_4\cdot\mathbf{v}-i\Gamma_{fe'})}\right\}. \tag{8}$$

The single double-sided Feynman diagram for scheme 2b corresponds to the following expression:

$$\chi^{(3)}_{2b}(-\omega_4,\omega_1,\omega_3,-\omega_2)$$
$$=\frac{N}{6\epsilon_0\hbar^3}\sum_{all\ M}\frac{\rho^{(0)}_{ii}\langle i|\boldsymbol{\epsilon}^*_4\cdot\boldsymbol{\mu}|e'\rangle\langle e'|\boldsymbol{\epsilon}^*_2\cdot\boldsymbol{\mu}|f\rangle\langle f|\boldsymbol{\epsilon}_3\cdot\boldsymbol{\mu}|e\rangle\langle e|\boldsymbol{\epsilon}_1\cdot\boldsymbol{\mu}|i\rangle}{(\omega_{ei}-\omega_1+\mathbf{k}_1\cdot\mathbf{v}-i\Gamma_{ei})[\omega_{fi}-\omega_1-\omega_3+(\mathbf{k}_1+\mathbf{k}_3)\cdot\mathbf{v}-i\Gamma_{fi}](\omega_{e'i}-\omega_4+\mathbf{k}_4\cdot\mathbf{v}-i\Gamma_{e'i})}. \tag{9}$$

Finally, the four double-sided Feynman diagrams, 3.1–3.4, represent the following expression for the nonlinear susceptibility for scheme 3:

$$\chi^{(3)}_{3}(-\omega_4,\omega_1,\omega_3,-\omega_2)$$
$$=\frac{N}{6\epsilon_0\hbar^3}\sum_{all\ M}\frac{\rho^{(0)}_{ii}\langle i'|\boldsymbol{\epsilon}^*_4\cdot\boldsymbol{\mu}|f\rangle\langle f|\boldsymbol{\epsilon}_3\cdot\boldsymbol{\mu}|i\rangle\langle i|\boldsymbol{\epsilon}^*_2\cdot\boldsymbol{\mu}|e\rangle\langle e|\boldsymbol{\epsilon}_1\cdot\boldsymbol{\mu}|i'\rangle}{(\omega_{ei'}-\omega_1+\mathbf{k}_1\cdot\mathbf{v}-i\Gamma_{ei'})[(\mathbf{k}_1-\mathbf{k}_2)\cdot\mathbf{v}-i\Gamma_{ii'}](\omega_{fi'}-\omega_4+\mathbf{k}_4\cdot\mathbf{v}-i\Gamma_{fi'})}$$
$$-\sum_{all\ M}\frac{\rho^{(0)}_{ii}\langle i'|\boldsymbol{\epsilon}^*_4\cdot\boldsymbol{\mu}|f\rangle\langle f|\boldsymbol{\epsilon}_3\cdot\boldsymbol{\mu}|i\rangle\langle i|\boldsymbol{\epsilon}^*_2\cdot\boldsymbol{\mu}|e\rangle\langle e|\boldsymbol{\epsilon}_1\cdot\boldsymbol{\mu}|i'\rangle}{(\omega_{ei}-\omega_2+\mathbf{k}_2\cdot\mathbf{v}+i\Gamma_{et})[(\mathbf{k}_1-\mathbf{k}_2)\cdot\mathbf{v}-i\Gamma_{ii'}](\omega_{fi'}-\omega_4+\mathbf{k}_4\cdot\mathbf{v}-i\Gamma_{fi'})}$$
$$-\sum_{all\ M}\frac{\rho^{(0)}_{ii}\langle f|\boldsymbol{\epsilon}_3\cdot\boldsymbol{\mu}|i\rangle\langle i|\boldsymbol{\epsilon}^*_2\cdot\boldsymbol{\mu}|e\rangle\langle e|\boldsymbol{\epsilon}_1\cdot\boldsymbol{\mu}|i'\rangle\langle i'|\boldsymbol{\epsilon}^*_4\cdot\boldsymbol{\mu}|f\rangle}{(\omega_{ei}-\omega_2+\mathbf{k}_2\cdot\mathbf{v}+i\Gamma_{ei})[\omega_{fe}-\omega_3+\omega_2+(\mathbf{k}_3-\mathbf{k}_2)\cdot\mathbf{v}-i\Gamma_{fe}](\omega_{fi'}-\omega_4+\mathbf{k}_4\cdot\mathbf{v}-i\Gamma_{fi'})}$$
$$+\sum_{all\ M}\frac{\rho^{(0)}_{ii}\langle f|\boldsymbol{\epsilon}_3\cdot\boldsymbol{\mu}|i\rangle\langle i|\boldsymbol{\epsilon}^*_2\cdot\boldsymbol{\mu}|e\rangle\langle e|\boldsymbol{\epsilon}_1\cdot\boldsymbol{\mu}|i'\rangle\langle i'|\boldsymbol{\epsilon}^*_4\cdot\boldsymbol{\mu}|f\rangle}{(\omega_{fi}-\omega_3+\mathbf{k}_3\cdot\mathbf{v}-i\Gamma_{fi})[\omega_{fe}-\omega_3+\omega_2+(\mathbf{k}_3-\mathbf{k}_2)\cdot\mathbf{v}-i\Gamma_{fe}](\omega_{fi'}-\omega_4+\mathbf{k}_4\cdot\mathbf{v}-i\Gamma_{fi'})}. \tag{10}$$

In Eqs. (6)–(10), N is the total number of absorbers, $\rho^{(0)}_{ii}$ is the initial density matrix element for the magnetic sublevel M_i of the level i and refers to the initial probability of the system being in that sublevel, the ket $|n\rangle$ and the bra $\langle n|$ represent the total molecular wave function for the quantum level characterized by total angular momentum $\mathbf{J}_n$, $\boldsymbol{\mu}$ is the electric dipole moment operator, $\hbar\omega_{nm}$ is the energy difference between the levels n and m (E_n-E_m), and $\mathbf{v}$ is the velocity vector of the absorbing molecule. The relaxation and dephasing rates Γ_{nm} are defined as

$$\Gamma_{nm}=\frac{(\Gamma_n+\Gamma_m)}{2}+\Gamma^{pd}_{nm}, \tag{11}$$

where $\Gamma_n=1/\tau_n$ with τ_n being the lifetime of the level n, and Γ^{pd}_{nm} is the pure collisional dephasing rate of the coherence between the levels n and m. Effects resulting from laser bandwidths and velocity changing collisions are not included in Eqs. (6)–(10), and to our knowledge have not been treated. Furthermore, effects arising from spontaneous emission, i.e., fluorescence optical pumping, are not included in Eqs. (6)–(10).

The TC-RFWM schemes 1a and 2a are often referred to as excited-state LIGS since the first two terms in Eq. (6) (diagrams 1a.1 and 1a.2) and Eq. (8) (diagrams 2a.1 and 2a.2) can be interpreted in terms of formation of and diffraction from excited-state gratings. In all experiments for which the PUMP and PROBE fields are present at the same time, however, the last term in each of Eqs. (6) and (8) (diagrams 1a.3 and 2a.3) also contributes to the signal. Each of these terms may be interpreted as a coherence between levels i and f that decays with the characteristic relaxation rate, Γ_{fi}. The TC-RFWM processes shown in Figs. 1(b) and 2(b) are completely described by this type of coherence. The TC-RFWM scheme 3 is also referred to as ground-state LIGS since the first two terms in Eq. (10) (diagrams 3.1 and 3.2) represent ground-state gratings. However, when both PUMP and PROBE pulses overlap in time there are two additional coherence terms (this time between levels e and f) that contribute to the RFWM signal. There are four double-sided Feynman diagrams for scheme 3, because both PUMP and PROBE transitions sample the initially populated level. Thus, any of the three input fields may interact first. By contrast, in the excited-state common schemes 1 and 2, only the PUMP transition samples the initially populated state so

that only fields 1 or 2 may interact first. The PROBE transition in schemes 1 and 2 connects two states that are initially unpopulated (by assumption) and thus field 3, which is always resonant with the PROBE transition, cannot interact first.

The general expressions in Eqs. (6)–(10) are derived from time-independent perturbation theory. Thus, strictly speaking, they only apply to the situation in which the perturbing fields overlap in time and have been applied long enough for the system to achieve a steady state. However, it is obvious that delaying the PROBE pulse with respect to the PUMP pulse in schemes 1a, 2a, and 3 decreases the signal contributions from the coherence terms. By contrast, RFWM signal can only be generated in schemes 1b and 2b when the PUMP and PROBE pulses overlap in time. The qualitative temporal aspects of schemes 1a and 1b are discussed in greater detail in Ref. 17. Diagrammatic perturbation theory may also be used to derive time-dependent expressions that explicitly treat the temporal evolution of the nonlinear susceptibility.

C. Spherical tensor solution for the four-photon matrix element products

In this section we seek to emphasize some key relations used in the evaluation of the four-photon matrix element products of Eqs. (6)–(10). We use a spherical tensor formalism that provides a well developed and efficient way of using the inherent symmetry of the system and allows the molecular and geometric factors to be separated from each other. The details of the method are presented elsewhere.[17,25] Below $\otimes$ refers to the tensor product and $\times$ refers to scalar multiplication.

We begin by noting that the four-photon matrix element product summed over the several degenerate sublevels is independent of the ordering of the matrix element product, e.g., for scheme 2b,

$$\sum_{all\ M} \langle i|\boldsymbol{\epsilon}_4^*\cdot\boldsymbol{\mu}|e'\rangle\langle e'|\boldsymbol{\epsilon}_2^*\cdot\boldsymbol{\mu}|f\rangle\langle f|\boldsymbol{\epsilon}_3\cdot\boldsymbol{\mu}|e\rangle\langle e|\boldsymbol{\epsilon}_1\cdot\boldsymbol{\mu}|i\rangle = \sum_{all\ M} \langle e|\boldsymbol{\epsilon}_1\cdot\boldsymbol{\mu}|i\rangle\langle i|\boldsymbol{\epsilon}_4^*\cdot\boldsymbol{\mu}|e'\rangle\langle e'|\boldsymbol{\epsilon}_2^*\cdot\boldsymbol{\mu}|f\rangle\langle f|\boldsymbol{\epsilon}_3\cdot\boldsymbol{\mu}|e\rangle. \tag{12}$$

Further, with the assumption that the initial state i is isotropic, the initial density matrix elements $\rho_u^{(0)}$ are constant and can be removed from the summations of Eqs. (6)–(10). Finally, we make the reasonable assumption that the relaxation rates, $\Gamma_{nn'}$, and the dipolar dephasing rates, Γ_{nm}, are independent of magnetic sublevel.[34] These two assumptions allow the separate evaluation of the numerators (four-photon matrix element products) and resonant denominators in Eqs. (6)–(10). The evaluation of the energy resonant denominators results in the RFWM spectral response, i.e., the line shape. The four-photon matrix element product, on the other hand, affects the intensity of the TC-RFWM signal and contains the effect of field polarizations.

The next step in the evaluation is to recognize that the total of the summation over projections onto the several degenerate sublevels of the level n constitutes a single projection operator indicated by

$$\sum_{M_n} |n\rangle\langle n| = 1. \tag{13}$$

Taking this into consideration, we express the general result for any four-photon matrix element product as

$$\begin{aligned}
&\sum_{all\ M} \langle a|\boldsymbol{\epsilon}_\chi\cdot\boldsymbol{\mu}|b\rangle\langle b|\boldsymbol{\epsilon}_\beta^*\cdot\boldsymbol{\mu}|c\rangle\langle c|\boldsymbol{\epsilon}_\gamma\cdot\boldsymbol{\mu}|d\rangle\langle d|\boldsymbol{\epsilon}_\delta^*\cdot\boldsymbol{\mu}|a\rangle \\
&= \sum_{M_n} \langle a|(\boldsymbol{\epsilon}_\chi\cdot\boldsymbol{\mu}_\chi)(\boldsymbol{\epsilon}_\beta^*\cdot\boldsymbol{\mu}_\beta)(\boldsymbol{\epsilon}_\gamma\cdot\boldsymbol{\mu}_\gamma)(\boldsymbol{\epsilon}_\delta^*\cdot\boldsymbol{\mu}_\delta)|a\rangle \\
&= \sum_K \left\{ \sum_{Q=-K}^{K} (-1)^Q [\boldsymbol{\epsilon}_\chi^{(1)}\otimes\boldsymbol{\epsilon}_\beta^{*(1)}]_Q^{(K)} [\boldsymbol{\epsilon}_\gamma^{(1)}\otimes\boldsymbol{\epsilon}_\delta^{*(1)}]_{-Q}^{(K)} \right. \\
&\quad \times \sum_{\alpha J} \sum_{\alpha' J'} \sum_{\alpha'' J''} (-1)^{J_a+3J} \begin{Bmatrix} J & J & K \\ 1 & 1 & J' \end{Bmatrix} \\
&\quad \times \begin{Bmatrix} J_a & J_a & K \\ 1 & 1 & J'' \end{Bmatrix} \langle \alpha_a J_a \| \mu_\chi^{(1)} \| \alpha' J' \rangle \langle \alpha' J' \| \mu_\beta^{(1)} \| \alpha J \rangle \\
&\quad \left. \times \langle \alpha J \| \mu_\gamma^{(1)} \| \alpha'' J'' \rangle \langle \alpha'' J'' \| \mu_\delta^{(1)} \| \alpha_a J_a \rangle \right\},
\end{aligned} \tag{14}$$

where the transition dipole moment operators have been subscripted for bookkeeping. Note in Eq. (14) that the only operator capable of connecting the bra $\langle a|$ to the ket $|a\rangle$ is a scalar. The evaluation of this operator, or number, is discussed in detail in Ref. 25, and the result is shown in Eq. (14). The effect of the matrix element reordering of the type in Eq. (12) is to alter the order of the angular momentum coupling in our treatment. Therefore we lose the physical significance of the $K=0$, 1, and 2 components of Eq. (14) as the contributions from (scalar) population, (dipolar) orientation, and (quadrupolar) alignment gratings, respectively. This aspect is discussed in detail in Ref. 35 and Sec. IV of Ref. 25.

In Eq. (14) the square of the reduced matrix element, $\langle \alpha_m J_m \| \mu^{(1)} \| \alpha_n J_n \rangle$ is the molecular line strength $S(\alpha_n J_n; \alpha_m J_m)$ of the $n \leftrightarrow m$ transition defined as

$$\begin{aligned}
S(\alpha_n J_n; \alpha_m J_m) &= |\langle \alpha_m J_m \| \mu^{(1)} \| \alpha_n J_n \rangle|^2 \\
&= |\langle \alpha_n J_n \| \mu^{(1)} \| \alpha_m J_m \rangle|^2,
\end{aligned} \tag{15}$$

where J is the total angular momentum quantum number and α represents all other quantum numbers, i.e., electronic and vibrational. Equation (15) is often expressed (see Ref. 30, pp. 283–290 and 312–315) as

$$S(\alpha_n J_n; \alpha_m J_m) = S^\alpha_{J_n J_m} S^R_{J_n J_m}, \tag{16}$$

where $S^\alpha_{J_n J_m}$ is the strength of the $\alpha_n \leftrightarrow \alpha_m$ vibronic band [in many cases simply the product of the Franck–Condon factor(s) and the square of the electronic transition moment], and $S^R_{J_n J_m}$ is the rotational line strength (Hönl–London fac-

tor). The terms in curly brackets in Eq. (14) are simply 6-j symbols and are tabulated on pages 169–171 of Ref. 30. The remaining factors of Eq. (14) are polarization tensor products that are evaluated in the Appendices of Refs. 17 and 25. The key aspect in evaluating the polarization tensor products is to recognize the symmetry of the product of two rank 1 tensors,

$$[T^{(1)}\otimes V^{(1)}]_Q^{(K)}=(-1)^K[V^{(1)}\otimes T^{(1)}]_Q^{(K)}. \tag{17}$$

The results for specific polarization cases in nearly collinear phase matching geometries are given in Table V of Ref. 25. Equations (14) and (17), used in conjunction with the expressions in the Appendix of Ref. 25, allow the evaluation of four-photon matrix element products for noncollinear phase matching geometries and mixed polarization states (elliptical light).

We provide one example, for scheme 2b, of the application of Eqs. (14) and (17) to the evaluation of a four-photon matrix element product. We have assumed that the excitation bandwidth is sufficiently narrow compared to the density of states (including Doppler broadening) of the absorbing species so that the interaction is exclusively between the degenerate magnetic sublevels of the levels involved in the one-photon resonant transitions. Therefore the electric dipole operators in the form of Eq. (14) appropriate to scheme 2b can only connect $\mathbf{J}_i\leftrightarrow\mathbf{J}_e$ and $\mathbf{J}_e\leftrightarrow\mathbf{J}_f$, i.e., $J\rightarrow J_e$, $J'\rightarrow J_i$, and $J''\rightarrow J_f$. This reduces Eq. (14) for scheme 2b to

$$\begin{aligned}\sum_{M_r}\langle e|(\boldsymbol{\epsilon}_1\cdot\boldsymbol{\mu}_1)(\boldsymbol{\epsilon}_4^*\cdot\boldsymbol{\mu}_4)(\boldsymbol{\epsilon}_2^*\cdot\boldsymbol{\mu}_2)(\boldsymbol{\epsilon}_3\cdot\boldsymbol{\mu}_3)|e\rangle&\\ =|\langle\alpha_eJ_e\|\mu^{(1)}\|\alpha_iJ_i\rangle|^2|\langle\alpha_fJ_f\|\mu^{(1)}\|\alpha_eJ_e\rangle|^2&\\ \times\sum_K\begin{Bmatrix}J_e & J_e & K\\ 1 & 1 & J_i\end{Bmatrix}\begin{Bmatrix}J_e & J_e & K\\ 1 & 1 & J_f\end{Bmatrix}&\\ \times\sum_{Q=-K}^{K}(-1)^Q[\boldsymbol{\epsilon}_1^{(1)}\otimes\boldsymbol{\epsilon}_4^{*(1)}]_Q^{(K)}[\boldsymbol{\epsilon}_2^{*(1)}\otimes\boldsymbol{\epsilon}_3^{(1)}]_{-Q}^{(K)},&\end{aligned} \tag{18}$$

where the labels on the electric dipole moment operator have been dropped. Applying Eq. (17) to Eq. (18) yields the following expression:

$$\begin{aligned}\sum_{M_r}\langle e|(\boldsymbol{\epsilon}_1\cdot\boldsymbol{\mu}_1)(\boldsymbol{\epsilon}_4^*\cdot\boldsymbol{\mu}_4)(\boldsymbol{\epsilon}_2^*\cdot\boldsymbol{\mu}_2)(\boldsymbol{\epsilon}_3\cdot\boldsymbol{\mu}_3)|e\rangle&\\ =|\langle\alpha_eJ_e\|\mu^{(1)}\|\alpha_iJ_i\rangle|^2|\langle\alpha_fJ_f\|\mu^{(1)}\|\alpha_eJ_e\rangle|^2&\\ \times\sum_K(-1)^K\begin{Bmatrix}J_e & J_e & K\\ 1 & 1 & J_i\end{Bmatrix}\begin{Bmatrix}J_e & J_e & K\\ 1 & 1 & J_f\end{Bmatrix}&\\ \times\sum_{Q=-K}^{K}(-1)^Q[\boldsymbol{\epsilon}_4^{*(1)}\otimes\boldsymbol{\epsilon}_1^{(1)}]_Q^{(K)}[\boldsymbol{\epsilon}_2^{*(1)}\otimes\boldsymbol{\epsilon}_3^{(1)}]_{-Q}^{(K)}.&\end{aligned} \tag{19}$$

Equation (19) is now in a form that can be easily evaluated using Table 4.1 of Ref. 30 and Table V of Ref. 25.

D. TC-RFWM signal expressions

The final step in the derivation of the macroscopic polarization is to average over the initial molecular distribution. For an isotropic gas all of the magnetic sublevels of a given level are equally populated, and no phase relation exists between levels. Therefore the average consists of integrating the expressions for $\boldsymbol{\chi}^{(3)}$ given in Eqs. (6)–(10) over the velocity distribution of the absorbing molecules, which is defined as follows:

$$N=\int N(\mathbf{v})d^3\mathbf{v}=N\int f(\mathbf{v})d^3\mathbf{v}. \tag{20}$$

In most experiments $f(\mathbf{v})$ is the normalized Maxwell–Boltzmann velocity distribution. Using Eqs (4)–(10), (14), (15), and (20) the expressions for the TC-RFWM signal intensity are evaluated. The TC-RFWM signal intensity for all schemes is expressed in the following form:

$$\begin{aligned}I_{\text{TC-RFWM}}\propto[N_i]^2[B_1]^2[B_3]^2I_1I_2I_3&\\ \times|\mathfrak{L}(\omega_1,\omega_3)|^2[G_F^T(\boldsymbol{\epsilon}_4,\boldsymbol{\epsilon}_1,\boldsymbol{\epsilon}_3,\boldsymbol{\epsilon}_2;J_i,J_e,J_f)]^2.&\end{aligned} \tag{21}$$

In Eq. (21) $N_i=N(2J_i+1)\rho_{ii}^{(0)}$ is the total population of the level i in the absence of applied fields. The terms B_1 and B_3 represent the Einstein coefficients for the PUMP and PROBE transitions, respectively, and are defined as follows:

$$B_1=B_{ie}(J_i,J_e)=\frac{\pi}{3\epsilon_0\hbar^2}\frac{|\langle\alpha_eJ_e\|\mu^{(1)}\|\alpha_iJ_i\rangle|^2}{2J_i+1}, \tag{22}$$

for all schemes,

$$B_3=B_{ef}(J_e,J_f)=\frac{\pi}{3\epsilon_0\hbar^2}\frac{|\langle\alpha_fJ_f\|\mu^{(1)}\|\alpha_eJ_e\rangle|^2}{2J_e+1}, \tag{23}$$

for schemes 1a, 1b, 2a, and 2b, and

$$B_3=B_{if}(J_i,J_f)=\frac{\pi}{3\epsilon_0\hbar^2}\frac{|\langle\alpha_fJ_f\|\mu^{(1)}\|\alpha_iJ_i\rangle|^2}{2J_i+1}, \tag{24}$$

for scheme 3. The $\mathfrak{L}(\omega_1,\omega_3)$ represent the total line shape functions expressed in terms of ω_1 and ω_3 that are obtained from the integration over the molecular velocity distribution defined in Eq. (20) of the resonant denominators given in Eqs. (6)–(10). Finally, the $G_F^T(\boldsymbol{\epsilon}_4,\boldsymbol{\epsilon}_1,\boldsymbol{\epsilon}_3,\boldsymbol{\epsilon}_2;J_i,J_e,J_f)$ are total geometric factors that depend solely on the polarization unit vectors of the electric fields $\boldsymbol{\epsilon}_j$ and the total angular momentum quantum numbers J_i, J_e, and J_f, and are defined as follows:

$$\begin{aligned}G_F^T(\boldsymbol{\epsilon}_4,\boldsymbol{\epsilon}_1,\boldsymbol{\epsilon}_3,\boldsymbol{\epsilon}_2;J_i,J_e,J_f)&\\ =(2J_e+1)\sum_K\begin{Bmatrix}J_e & J_e & K\\ 1 & 1 & J_i\end{Bmatrix}\begin{Bmatrix}J_e & J_e & K\\ 1 & 1 & J_f\end{Bmatrix}&\\ \times\sum_{Q=-K}^{K}(-1)^Q[\boldsymbol{\epsilon}_4^{*(1)}\otimes\boldsymbol{\epsilon}_3^{(1)}]_Q^{(K)}[\boldsymbol{\epsilon}_2^{*(1)}\otimes\boldsymbol{\epsilon}_1^{(1)}]_{-Q}^{(K)}&\end{aligned} \tag{25}$$

for scheme 1a;

$$G_F^T(\boldsymbol{\epsilon}_4,\boldsymbol{\epsilon}_1,\boldsymbol{\epsilon}_3,\boldsymbol{\epsilon}_2;J_i,J_e,J_f)$$
$$=(2J_e+1)\sum_K \begin{Bmatrix} J_e & J_e & K \\ 1 & 1 & J_i \end{Bmatrix}\begin{Bmatrix} J_e & J_e & K \\ 1 & 1 & J_f \end{Bmatrix}$$
$$\times\sum_{Q=-K}^{K}(-1)^Q[\boldsymbol{\epsilon}_4^{*(1)}\otimes\boldsymbol{\epsilon}_1^{(1)}]_Q^{(K)}[\boldsymbol{\epsilon}_2^{*(1)}\otimes\boldsymbol{\epsilon}_3^{(1)}]_{-Q}^{(K)} \quad (26)$$

for scheme 1b;

$$G_F^T(\boldsymbol{\epsilon}_4,\boldsymbol{\epsilon}_1,\boldsymbol{\epsilon}_3,\boldsymbol{\epsilon}_2;J_i,J_e,J_f)$$
$$=(2J_e+1)\sum_K (-1)^K\begin{Bmatrix} J_e & J_e & K \\ 1 & 1 & J_i \end{Bmatrix}$$
$$\times\begin{Bmatrix} J_e & J_e & K \\ 1 & 1 & J_f \end{Bmatrix}\sum_{Q=-K}^{K}(-1)^Q[\boldsymbol{\epsilon}_4^{*(1)}\otimes\boldsymbol{\epsilon}_3^{(1)}]_Q^{(K)}$$
$$\times[\boldsymbol{\epsilon}_2^{*(1)}\otimes\boldsymbol{\epsilon}_1^{(1)}]_{-Q}^{(K)} \quad (27)$$

for scheme 2a;

$$G_F^T(\boldsymbol{\epsilon}_4,\boldsymbol{\epsilon}_1,\boldsymbol{\epsilon}_3,\boldsymbol{\epsilon}_2;J_i,J_e,J_f)$$
$$=(2J_e+1)\sum_K (-1)^K\begin{Bmatrix} J_e & J_e & K \\ 1 & 1 & J_i \end{Bmatrix} \quad (28)$$
$$\times\begin{Bmatrix} J_e & J_e & K \\ 1 & 1 & J_f \end{Bmatrix}\sum_{Q=-K}^{K}(-1)^Q[\boldsymbol{\epsilon}_4^{*(1)}\otimes\boldsymbol{\epsilon}_1^{(1)}]_Q^{(K)}$$
$$\times[\boldsymbol{\epsilon}_2^{*(1)}\otimes\boldsymbol{\epsilon}_3^{(1)}]_{-Q}^{(K)}$$

for scheme 2b; and

$$G_F^T(\boldsymbol{\epsilon}_4,\boldsymbol{\epsilon}_1,\boldsymbol{\epsilon}_3,\boldsymbol{\epsilon}_2;J_i,J_e,J_f)$$
$$=(2J_i+1)\sum_K \begin{Bmatrix} J_i & J_i & K \\ 1 & 1 & J_e \end{Bmatrix}\begin{Bmatrix} J_i & J_i & K \\ 1 & 1 & J_f \end{Bmatrix}$$
$$\times\sum_{Q=-K}^{K}(-1)^Q[\boldsymbol{\epsilon}_4^{*(1)}\otimes\boldsymbol{\epsilon}_3^{(1)}]_Q^{(K)}[\boldsymbol{\epsilon}_2^{*(1)}\otimes\boldsymbol{\epsilon}_1^{(1)}]_{-Q}^{(K)} \quad (29)$$

for scheme 3.

The weak-field signal expression in Eq. (21) is the key result of this section and expresses the TC-RFWM signal intensity as a product of a concentration term, $[N_i]^2$, a one-photon molecular term, $[B_1]^2[B_3]^2$, a line shape function, $|\mathfrak{L}(\omega_1,\omega_3)|^2$, and a laboratory-frame geometric factor, $[G_F^T(\boldsymbol{\epsilon}_4,\boldsymbol{\epsilon}_1,\boldsymbol{\epsilon}_3,\boldsymbol{\epsilon}_2;J_i,J_e,J_f)]^2$. These quantities relate to different aspects of the experimental arrangement and the molecular properties. Equation (21) is a powerful result because those factors which depend on the interaction of the molecule with the fields in the molecular frame are separated from those factors relating to the interaction of the molecule with the fields in the laboratory frame. This separation greatly simplifies the calculation and facilitates the practical analysis of TC-RFWM spectra.

The dynamics of the electric dipole interaction are contained in the Einstein coefficients which describe the strength of the interaction of the molecule with the excitation fields in the molecular frame, i.e., the greater the line strength of the molecular transition, the larger the TC-RFWM signal intensity. These coefficients can be related to other molecular parameters such as the absorption cross section, the oscillator strength, the line strength, the spontaneous emission lifetime, and the transition-dipole moment.[36] The line shape function depends on inhomogeneous broadening due to molecular velocity effects and on homogeneous broadening due either to collisions or intramolecular nonradiative processes (predissociation, internal conversion, etc.). In evaluating Eq. (21), we make the reasonable assumption that for a dipolar transition $\Gamma_{n'm'}=\Gamma_{n'm}=\Gamma_{nm'}=\Gamma_{nm}$, i.e., that only one optical relaxation rate need be considered for each transition.[34,37] Furthermore, we assume that the degenerate magnetic sublevels of each distinct level i, e, and f relax independently and equally which is equivalent to stating that the relaxation of the multipole moments of the total angular momentum distribution relax independently and equally. In this case, $1/\Gamma_{nn'}=1/\Gamma_n=\tau_n$ where τ_n is the lifetime of the nth level.

In general, the total line shape function involves the velocity integration described above, and therefore, cannot be expressed in a simple analytical form. The explicit evaluation of this function for each TC-RFWM process under all relaxation and velocity regimes is beyond the scope of this paper. In the limiting case of stationary, noninteracting molecules, however, the line shape functions can be reduced to simple expressions. With the additional assumption that the intramolecular relaxation dominates over radiative processes, we have shown that the line shape function for tuning ω_3 (with ω_1 on resonance) is a simple Lorentzian for schemes 1a and 1b.[17] This simplification can also be demonstrated for schemes 2a and 2b. The stationary, noninteracting molecule limit is useful for free-jet expansions in which collisional effects and residual velocity distributions are often negligible.

The spatial aspects of the molecular distribution with respect to the laboratory frame are described by the geometric factors, $G_F^T(\boldsymbol{\epsilon}_4,\boldsymbol{\epsilon}_1,\boldsymbol{\epsilon}_3,\boldsymbol{\epsilon}_2;J_i,J_e,J_f)$, which depend on the polarization vectors of the electric fields and the level degeneracies. The simple analytical expressions for the geometric factors for the TC-RFWM schemes in Figs. 1–3 are evaluated and the results shown in Tables I–III, respectively, for the allowed polarization configurations of linearly polarized light in nearly collinear phase matching geometries. We have chosen the space-fixed Z axis as the propagation axis for the four fields. The collinear beam approximation in turn restricts the electric fields to lie in the space-fixed XY plane. There are four possible orthogonal linear polarization configurations, $YYYY$, $YXYX$, $YYXX$, and $YXXY$ (permuting X and Y has no effect on the geometric factors). Note that for each scheme there are two configurations in which the polarization of the signal beam is orthogonal to that of the input beam at the same frequency. These configurations offer the practical advantage of enhanced rejection of scattered light at the signal frequency.[17] For each polarization configuration there are nine possible combinations of two-color rotational branch combinations, i.e., there are nine possible paths denoted by $J_i\rightarrow J_e\rightarrow J_f$, and hence there are a total of 36 geometric factors for each TC-RFWM scheme. We label both

TABLE I. Total geometric factors $G_F^T(\boldsymbol{\epsilon}_4,\boldsymbol{\epsilon}_1,\boldsymbol{\epsilon}_3,\boldsymbol{\epsilon}_2;J_i,J_e,J_f)$ for TC-RFWM schemes 1a and 1b appropriate to SEP spectroscopy depicted in Fig. 1. The factors are given for each double-resonance branch combination in terms of J_i, where the subscript has been dropped for clarity. Interchanging $X \leftrightarrow Y$ does not affect the geometric factors.

	Polarization configuration $(\boldsymbol{\epsilon}_4\boldsymbol{\epsilon}_1\boldsymbol{\epsilon}_3\boldsymbol{\epsilon}_2)$[b]			
Branch combination[a]	(a) *YYYY* (b) *YYYY*	(a) *YXYX* (b) *YYXX*	(a) *YYXX* (b) *YXYX*	(a) *YXXY* (b) *YXXY*
PP	$\frac{2}{15}\frac{(J^2+1/4)}{(J^2+1/2J)}$	$\frac{1}{10}\frac{(J^2+5/6J-1/6)}{(J^2+1/2J)}$	$\frac{1}{10}\frac{(J^2-5/6J-1/6)}{(J^2+1/2J)}$	$-\frac{1}{15}\frac{(J^2-1)}{(J^2+1/2J)}$
QQ	$\frac{1}{5}\frac{(J^2+J-1/3)}{(J^2+J)}$	$\frac{1}{15}\frac{(J^2+J+1/2)}{(J^2+J)}$	$\frac{1}{15}\frac{(J^2+J+1/2)}{(J^2+J)}$	$\frac{1}{15}\frac{(J^2+J-2)}{(J^2+J)}$
RR	$\frac{2}{15}\frac{(J^2+2J+5/4)}{(J^2+3/2J+1/2)}$	$\frac{1}{10}\frac{(J^2+7/6J)}{(J^2+3/2J+1/2)}$	$\frac{1}{10}\frac{(J^2+17/6J+5/3)}{(J^2+3/2J+1/2)}$	$-\frac{1}{15}\frac{(J^2+2J)}{(J^2+3/2J+1/2)}$
PQ	$-\frac{1}{15}\frac{(J+1)}{J}$	$-\frac{2}{15}\frac{(J-1/4)}{J}$	$\frac{1}{30}\frac{(J+1)}{J}$	$\frac{1}{30}\frac{(J-4)}{J}$
QP	$-\frac{1}{15}\frac{(J+2)}{(J+1)}$	$-\frac{2}{15}\frac{(J+3/4)}{(J+1)}$	$\frac{1}{30}\frac{(J+2)}{(J+1)}$	$\frac{1}{30}\frac{(J-3)}{(J+1)}$
RQ	$-\frac{1}{15}\frac{J}{(J+1)}$	$-\frac{2}{15}\frac{(J+5/4)}{(J+1)}$	$\frac{1}{30}\frac{J}{(J+1)}$	$\frac{1}{30}\frac{(J+5)}{(J+1)}$
QR	$-\frac{1}{15}\frac{(J-1)}{J}$	$-\frac{2}{15}\frac{(J+1/4)}{J}$	$\frac{1}{30}\frac{(J-1)}{J}$	$\frac{1}{30}\frac{(J+4)}{J}$
PR or **RP**	$\frac{2}{15}$	$\frac{1}{10}$	$-\frac{1}{15}$	$\frac{1}{10}$

[a]Both PUMP and DUMP rotational branches are labeled as upward transitions, i.e., $J_e \leftarrow J_i$ and $J_e \leftarrow J_f$.
[b]The (a) and (b) labels refer to TC-RFWM schemes 1a and 1b, respectively.

TABLE II. Total geometric factors $G_F^T(\boldsymbol{\epsilon}_4,\boldsymbol{\epsilon}_1,\boldsymbol{\epsilon}_3,\boldsymbol{\epsilon}_2,J_i,J_e,J_f)$ for TC-RFWM schemes 2a and 2b appropriate to excited-state double-resonance spectroscopy depicted in Fig. 2. The factors are given for each double-resonance branch combination in terms of J_i, where the subscript has been dropped for clarity. Interchanging $X \leftrightarrow Y$ does not affect the geometric factors.

	Polarization configuration $(\boldsymbol{\epsilon}_4\boldsymbol{\epsilon}_1\boldsymbol{\epsilon}_3\boldsymbol{\epsilon}_2)$[b]			
Branch combination[a]	(a) *YYYY* (b) *YYYY*	(a) *YXYX* (b) *YYXX*	(a) *YXXY* (b) *YXXY*	(a) *YYXX* (b) *YXYX*
PR	$\frac{2}{15}\frac{(J^2+1/4)}{(J^2+1/2J)}$	$\frac{1}{10}\frac{(J^2+5/6J-1/6)}{(J^2+1/2J)}$	$\frac{1}{10}\frac{(J^2-5/6J-1/6)}{(J^2+1/2J)}$	$-\frac{1}{15}\frac{(J^2-1)}{(J^2+1/2J)}$
QQ	$\frac{1}{5}\frac{(J^2+J-1/3)}{(J^2+J)}$	$\frac{1}{15}\frac{(J^2+J+1/2)}{(J^2+J)}$	$\frac{1}{15}\frac{(J^2+J+1/2)}{(J^2+J)}$	$\frac{1}{15}\frac{(J^2+J-2)}{(J^2+J)}$
RP	$\frac{2}{15}\frac{(J^2+2J+5/4)}{(J^2+3/2J+1/2)}$	$\frac{1}{10}\frac{(J^2+7/6J)}{(J^2+3/2J+1/2)}$	$\frac{1}{10}\frac{(J^2+17/6J+5/3)}{(J^2+3/2J+1/2)}$	$-\frac{1}{15}\frac{(J^2+2J)}{(J^2+3/2J+1/2)}$
PQ	$-\frac{1}{15}\frac{(J+1)}{J}$	$-\frac{2}{15}\frac{(J-1/4)}{J}$	$\frac{1}{30}\frac{(J+1)}{J}$	$\frac{1}{30}\frac{(J-4)}{J}$
QR	$-\frac{1}{15}\frac{(J+2)}{(J+1)}$	$-\frac{2}{15}\frac{(J+3/4)}{(J+1)}$	$\frac{1}{30}\frac{(J+2)}{(J+1)}$	$\frac{1}{30}\frac{(J-3)}{(J+1)}$
RQ	$-\frac{1}{15}\frac{J}{(J+1)}$	$-\frac{2}{15}\frac{(J+5/4)}{(J+1)}$	$\frac{1}{30}\frac{J}{(J+1)}$	$\frac{1}{30}\frac{(J+5)}{(J+1)}$
QP	$-\frac{1}{15}\frac{(J-1)}{J}$	$-\frac{2}{15}\frac{(J+1/4)}{J}$	$\frac{1}{30}\frac{(J-1)}{J}$	$\frac{1}{30}\frac{(J+4)}{J}$
PP or **RR**	$\frac{2}{15}$	$\frac{1}{10}$	$-\frac{1}{15}$	$\frac{1}{10}$

[a]Both PUMP and PROBE rotational branches are labeled as upward transitions, i.e., $J_e \leftarrow J_i$ and $J_f \leftarrow J_e$.
[b]The (a) and (b) labels refer to TC-RFWM schemes 2a and 2b, respectively.

TABLE III. Total geometric factors $G_F^T(\epsilon_4,\epsilon_1,\epsilon_3,\epsilon_2;J_i,J_e,J_f)$ for TC-RFWM scheme 3 appropriate to ground-state double-resonance spectroscopy depicted in Fig. 3. The factors are given for each double-resonance branch combination in terms of J_i, where the subscript has been dropped for clarity. Interchanging $X \leftrightarrow Y$ does not affect the geometric factors.

Branch combination[a]	Polarization configuration ($\epsilon_4\epsilon_1\epsilon_3\epsilon_2$)			
	YYYY	*YXYX*	*YYXX*	*YXXY*
RR	$\frac{2}{15}\frac{(J^2+2J+5/4)}{(J^2+5/2J+3/2)}$	$\frac{1}{10}\frac{(J^2+17/6J+5/3)}{(J^2+5/2J+3/2)}$	$\frac{1}{10}\frac{(J^2+7/6J)}{(J^2+5/2J+3/2)}$	$-\frac{1}{15}\frac{(J^2+2J)}{(J^2+5/2J+3/2)}$
QQ	$\frac{1}{5}\frac{(J^2+J-1/3)}{(J^2+J)}$	$\frac{1}{15}\frac{(J^2+J+1/2)}{(J^2+J)}$	$\frac{1}{15}\frac{(J^2+J+1/2)}{(J^2+J)}$	$\frac{1}{15}\frac{(J^2+J-2)}{(J^2+J)}$
PP	$\frac{2}{15}\frac{(J^2+1/4)}{(J^2-1/2J)}$	$\frac{1}{10}\frac{(J^2-5/6J-1/6)}{(J^2-1/2J)}$	$\frac{1}{10}\frac{(J^2+5/6J-1/6)}{(J^2-1/2J)}$	$-\frac{1}{15}\frac{(J^2-1)}{(J^2-1/2J)}$
RQ or **QR**	$-\frac{1}{15}\frac{(J+2)}{(J+1)}$	$-\frac{2}{15}\frac{(J+3/4)}{(J+1)}$	$\frac{1}{30}\frac{(J+2)}{(J+1)}$	$\frac{1}{30}\frac{(J-3)}{(J+1)}$
PQ or **QP**	$-\frac{1}{15}\frac{(J-1)}{J}$	$-\frac{2}{15}\frac{(J+1/4)}{J}$	$\frac{1}{30}\frac{(J-1)}{J}$	$\frac{1}{30}\frac{(J+4)}{J}$
PR or **RP**	$\frac{2}{15}$	$\frac{1}{10}$	$-\frac{1}{15}$	$\frac{1}{10}$

[a]Both PUMP and PROBE rotational branches are labeled as upward transitions, i.e., $J_e \leftarrow J_i$ and $J_f \leftarrow J_i$.

resonant transitions as upward transitions in Tables I–III and give all geometric factors in terms of J_i. The apparent reduction in the number of unique factors for scheme 3 (Table III) relative to those for schemes 1 and 2 (Tables I and II) is due to the fact that i is the common level for scheme 3. If the geometric factors for schemes 1 and 2 were given in terms of the angular momentum of their common level, J_e, the number of unique factors in Tables I and II would be identical to those in Table III.

In Fig. 4 we plot the total geometric factors for schemes 2a and 2b for the four polarization configurations in the case of an R-branch PUMP transition. As these plots illustrate, the geometric factors vary significantly at low J ($J<5$) but rapidly approach a high-J limit ($J>5$). Even in the high-J limit, however, there are still pronounced differences in the geometric factors for different branch combinations or polarization configurations. For example, the *YYXX* configuration for scheme 1a greatly enhances the *RR* combination over *RQ* and, to a lesser extent *RP* [Fig. 4(c)]. Conversely, the *YXXY* configuration for scheme 1a enhances the *RP* combination over *RQ* and *RR*. Note also that the sign of $G_F^T(\epsilon_4,\epsilon_1,\epsilon_3,\epsilon_2;J_i,J_e,J_f)$ may be positive or negative. This apparent phase has no bearing on isolated lines, since the signal scales as the square of the geometric factor, but can be manifested in the interference between overlapping lines whose geometric factors have different signs.[17]

III. OTHER CONSIDERATIONS

A. Interaction length

Equation (21) does not include a term that accounts for the length of the interaction, L, of the fields with the medium. Because the nonlinear polarization is proportional to $(ik_4L/2\epsilon_0)\wp^{(3)}_{\mathrm{RFWM}}$ (see Ref. 33, pp. 217 and 218), the TC-RFWM signal is proportional to L^2. Experimentally L is determined either by the crossing angle of the fields or by the dimensions of the nonlinear medium. Therefore, in some cases, the TC-RFWM signal can be increased by elongating the interaction length without a change in the number density. However, an increase in the interaction length has a detrimental effect on the phase matching bandwidth for TC-RFWM which scales as $1/L^2$.[16,20]

B. Spontaneous emission

In the event that spontaneous emission is a dominant relaxation process, the RFWM signal expressions presented in Sec. II do not apply. A full treatment considering the influence of spontaneous emission necessitates the inclusion of additional terms that depend on K, because the spontaneous emission rate depends on the magnetic sublevel.[37–39] Hence, the assumption made in Sec. II that the multipole moments of the total angular momentum distribution relax equally is not valid. In many experiments, however, the lifetimes of the states involved are dominated by nonradiative intermolecular or intramolecular processes (collisions, predissociation, internal conversion, etc.) and the effects of spontaneous emission are negligible. Even in those cases where the relaxation is dominated by radiative processes, the expressions presented herein provide qualitative information, reproduce general spectroscopic trends, and aid in assigning spectra.

C. Hyperfine depolarization

In the absence of collisions, the rotational angular momentum **J**, couples to the nuclear spin angular momentum **I** to form the total angular momentum **F** so that the prepared direction of **J** in the laboratory frame is lost to some degree (depolarized).[30,40,41] This directional blurring obviously influences the geometric factors related to the distribution of **J** in the laboratory frame. If the magnitude of **J** is substantially larger than the magnitude of **I** (typically I takes values up to

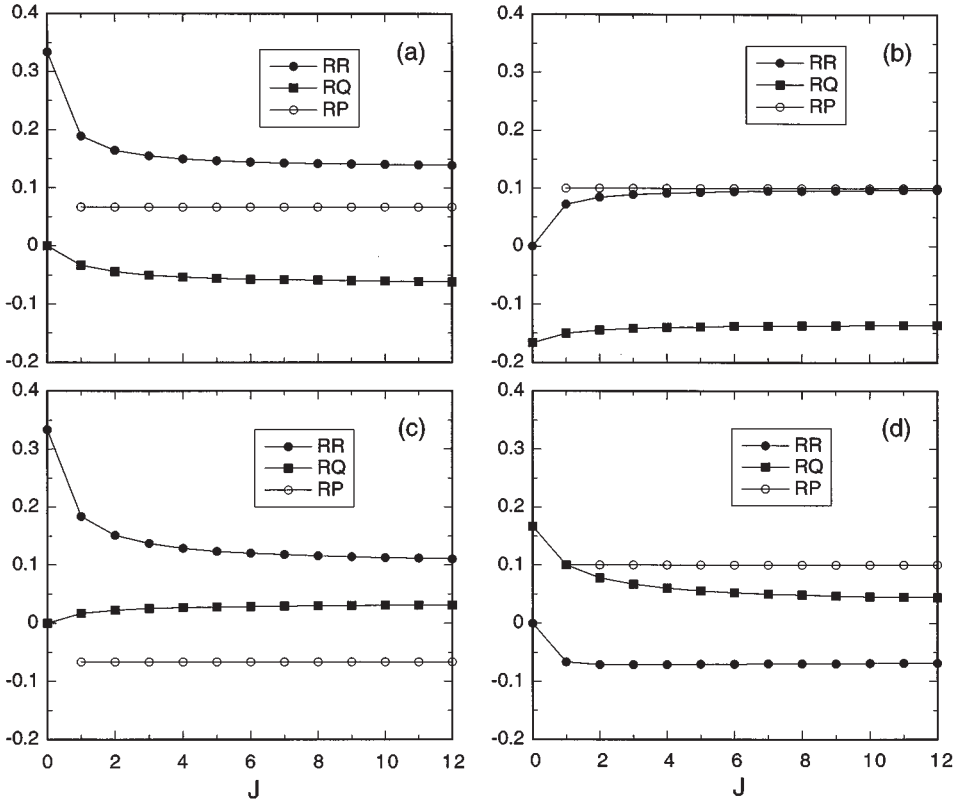

FIG. 4. Representative total geometric factors for the TC-RFWM schemes appropriate to SEP spectroscopy (schemes 1a and 1b) with an *R*-branch PUMP transition and various polarization configurations: (a) *YYYY*, (b) *YXYX* for 1a or *YYXX* for 1b, (c) *YYXX* for 1a or *YXYX* for 1b, and (d) *YXXY*.

about 5/2), **J** and **F** will be close to parallel, and the hyperfine depolarization will be small. In addition, if the optical excitation time (laser pulse duration) or the total relaxation time (collisions, intramolecular processes, etc.) are much faster than the precessional period of **J** about **F** (usually tens of nanoseconds or longer), then essentially no hyperfine precession occurs, and the hyperfine depolarization is small even for $J \sim I$. If neither of these conditions are met, however, the hyperfine depolarization can be significant and should be included for quantitative analysis.

D. Anisotropic initial state

The signal expressions presented in Sec. II were derived under the assumption that the initial state is isotropic, i.e., that all magnetic sublevels are equally populated and that no phase relation exists among them. If the initial state is a nascent product of a photolysis or chemical reaction then, in general, it will be anisotropic.[30,42] Anisotropy is manifested as either molecular orientation, a nonzero $K=$odd component of the total angular momentum distribution, or as alignment, a nonzero $K=$even component of the total angular momentum distribution. To reduce RFWM signals to relative populations in these cases, the geometric factors derived here cannot be applied, and the initial anisotropy must be properly accounted for in the sum over the initial density matrix elements, $\rho_{ii}^{(0)}$, given in Eqs. (6)–(10).

E. Unequal relaxation of the multipole moments

In the event that the multipole moments of the total angular momentum distribution, i.e., the population, the orientation, and the alignment, do not relax equally, the expression presented for the TC-RFWM signal intensity in Sec. II does not apply. Such conditions can arise from fluorescence optical pumping and reorienting (elastic) collisions. We have recently observed experimental conditions for which the later case applied.[35]

F. Overlapping transitions

If the spectral separation of two (or more) transitions is comparable to their total linewidths, then coherent addition of the $\boldsymbol{\chi}^{(3)}$ amplitudes for each of the transitions is necessary. Equations (6)–(10), in conjunction with Eq. (14), may be used to calculate the contribution of each transition to $\wp_{\mathrm{RFWM}}^{(3)}$ and subsequently to derive expressions similar to Eq. (21) that describe spectrally congested regions with overlapping branches. Applications of this type of analysis are presented for DFWM in Ref. 43 and for TC-RFWM as applied to SEP in Ref. 17. It is also possible to treat cases in which one of the states in the TC-RFWM process is a continuum, e.g., if state *f* in schemes 2a and 2b is a photoionization continuum. The key is to appropriately coherently sum the transition dipoles, which might include both bound-free transitions and

intramolecular interferences between sharp resonances and a continuum (i.e., Fano-type profiles), for all channels that contribute at a given energy.

G. Saturation

The effects of saturation on RFWM signal intensities have not been expressed analytically. However, for DFWM[1,4,44] a reduced line strength dependence is observed with increasing field intensity and the geometric factors vary slowly with field intensity but remain reasonably accurate even under saturated conditions. Williams, Zare, and Rahn[4] found that the geometric factors for DFWM remain accurate to within 30% at up to twice the saturation intensity and Lehr *et al.*[44] have demonstrated similar accuracy at up to five times the saturation intensity. In the weak-field limit, the RFWM signal is dependent on the spatial anisotropy of the total angular momentum distribution induced by the three input fields. Therefore the applicability of the geometric factors at saturating field intensities implies that the relative anisotropy of the total angular momentum represented by the total geometric factors persists to a large degree as the field intensity increases. This effect is similar to that expected for saturated laser-induced fluorescence measured with different polarization configurations.[45]

H. Other grating contributions

Our description of TC-RFWM assumes that only resonant four-wave mixing processes contribute to the observed signal. For some experimental conditions, however, other types of laser-induced grating phenomena[19] can scatter light along the RFWM phase matching direction and may dominate the signal of interest. Likely sources of additional signal in high-density gases or liquids in which collisional relaxation is rapid are thermal gratings.[14,46] Thermal gratings arise from the relaxation of excited-state population gratings that are formed from the intensity grating created by crossing two beams of identical frequency and polarization. The relaxation (heating) produces a spatially modulated density in the sample which translates into a spatial modulation in the real part of the refractive index. For example, thermal gratings from excited-state population gratings can be formed by ω_1 and ω_2 in schemes 1a, 2a, and 3 in the $YYYY$ and $YXYX$ configurations. In TC-RFWM thermal gratings produce nonresonant backgrounds since their diffraction efficiency is independent of whether ω_3 is resonant with the probe transition. Another intensity grating effect observed at high laser intensities is an electrostrictive grating that results from an electric-field induced modulation in the density.[47]

Thermal and electrostrictive gratings can result only from the interference of two fields that have the same polarization. Fields with orthogonal polarizations do not produce such effects, because there is no spatial modulation of the field intensity (only its polarization is spatially modulated)[48,49] Thus, the $YYXX$ and $YXXY$ configurations for schemes 1a, 2a, and 3 do not produce thermal or electrostrictive gratings. If the molecule is optically active (chiral), however, then circular-dichroism induced thermal gratings can be formed with orthogonally polarized fields.[50] Finally, schemes 1b and 2b cannot produce thermal gratings since they do not involve excited-state population gratings.

I. Sensitivity

The recent applications of DFWM and TC-RFWM to molecular systems have yielded detection limits for these RFWM techniques that fall in the range of 10^9–10^{12} molecules cm^{-3} per quantum state depending on the oscillator strengths of the transitions involved and on the extent of saturation.[3,5,12] RFWM techniques will always be limited, however, by their quadratic dependence on number density that is illustrated for TC-RFWM in Eq. (21).

In TC-RFWM the experimentalist has a choice of which transition is resonant with the signal field, i.e., a choice between schemes 1a (2a) and 1b (2b), and the choice of pump and probe transitions for scheme 3. Equation (21) shows that this choice is irrelevant in the weak-field limit, because the signal scales as the square of the Einstein coefficients for the pump and probe transitions. As a practical rule, however, it is always advisable to have the signal field in resonance with the stronger of the two transitions. In that manner both the transition dipole and intensity dependencies of the TC-RFWM signal for the weaker transition can be reduced significantly through saturation without affecting the scattered light level determined by the intensity of the single input field at the same frequency as the signal field. This advantage has been experimentally demonstrated using SEP scheme 2a in the commonly occurring case in which the PUMP transition is much stronger than the PROBE (DUMP) transition. Finally, the scattered light background can be further reduced in TC-RFWM, thus increasing the sensitivity, through the use of polarization configurations in which the signal field is orthogonally polarized to the single input field at the same frequency.[17] These configurations are $YYXX$ and $YXXY$ for schemes 1a, 2a, and 3 and $YXYX$ and $YXXY$ for schemes 1b and 2b.

IV. CONCLUSIONS

This paper demonstrates the potential of TC-RFWM to become another powerful tool for double-resonance molecular spectroscopy. We used time-independent, diagrammatic perturbation theory in conjunction with a spherical tensor analysis to derive weak-field signal expressions for each possible application of TC-RFWM to double-resonance spectroscopy. These include applications to SEP via schemes 1a and 1b presented in Fig. 1, to excited-state double resonances (or OODR) via schemes 2a and 2b shown in Fig. 2, and to ground-state double resonance (or hole burning) given in Fig. 3. The expressions are embodied in Eq. (21) and the associated definitions given in Eqs. (22)–(29).

Our theoretical approach, which is an extension of our previous work on DFWM[25] and TC-RFWM as applied to SEP,[17] completely separates the molecular properties (line strengths, relaxation rates, etc.) from laboratory frame factors determined entirely by the polarizations of the input fields and the total angular momenta of the three levels involved in

the TC-RFWM process. The total geometric factors for each TC-RFWM process are reduced to simple analytical expressions and are evaluated in Tables I–III. These factors are intended to facilitate the practical analysis of the effects of polarization in TC-RFWM spectra. Relaxation effects are described through the total line shape function for each TC-RFWM process. These effects depend critically on the nature of the intra- and intermolecular relaxation processes and on the molecular velocity distribution, and we have outlined the general approach for the evaluation of line shape functions. Finally, we have presented a list of additional considerations that should be addressed prior to applying TC-RFWM and using the weak-field signal expressions to analyze TC-RFWM spectra.

The strong polarization effects inherent in TC-RFWM provide several important benefits. Besides using certain polarization configurations to eliminate thermal gratings and reduce scattered light background, which are two important experimental advantages, the appropriate use of polarization effects can be used to greatly enhance certain rotational branch combinations (as shown in Fig. 4). This use is particularly advantageous for low J, for which spatial anisotropy effects are most strongly manifested. These types of rotational branch enhancements, when combined with the already formidable simplifying power arising from the double-resonance nature of TC-RFWM, provide substantial leverage in making rotational assignments in congested spectra. This aspect of TC-RFWM is particularly useful for large molecules and/or high temperatures and has only recently begun to be exploited.

ACKNOWLEDGMENTS

Work at Sandia is supported by the U.S. Department of Energy, Office of Basic Energy Sciences, Division of Chemical Sciences.

[1] R. L. Farrow and D. J. Rakestraw, Science **257**, 1894 (1992).
[2] P. Ewart and S. V. O'Leary, Opt. Lett. **11**, 279 (1986).
[3] T. Dreier and D. J. Rakestraw, Opt. Lett. **15**, 72 (1990), Appl. Phys. B **50**, 479 (1990).
[4] S. Williams, R. N. Zare, and L. A. Rahn, J. Chem. Phys. **101**, 1093 (1994).
[5] S. Williams, D. S. Green, S. Sethuraman, and R. N. Zare, J. Am. Chem. Soc. **114**, 9122 (1992).
[6] S. Williams, L. A. Rahn, P. H. Paul, J. W. Forsman, and R. N. Zare, Opt. Lett. **19**, 1 (1994).
[7] T. G. Owano, C. H. Kruger, D. S. Green, S. Williams, and R. N. Zare, Diamond Relat. Mater. **2**, 661 (1993).
[8] D. S. Green, T. G. Owano, S. Williams, D. G. Goodwin, R. N. Zare, and C. H. Kruger, Science **259**, 1726 (1993).
[9] T. G. Owano, E. H. Wahl, C. H. Kruger, D. S. Green, and R. N. Zare, Proceedings of the 11th International Symposium on Plasma Chemistry, 1993 (unpublished), p. 416.
[10] R. L. Abrams, J. F. Lam, R. C. Lind, D. G. Steel, and P. F. Liao, in *Optical Phase Conjugation*, edited by R. A. Fisher (Academic, San Diego, 1983), p. 211.
[11] Q. Zhang, S. A. Kandel, T. A. W. Wasserman, and P. H. Vaccaro, J. Chem. Phys. **96**, 1640 (1992).
[12] P. H. Vaccaro, in *Molecular Dynamics and Spectroscopy by Stimulated Emission Pumping*, edited by H.-L. Dai and R. W. Field, Advances in Physical Chemistry, edited by C.-Y. Ng (World Scientific, Singapore, 1994).
[13] E. F. McCormack, S. T. Pratt, P. M. Dehmer, and J. L. Dehmer, Chem. Phys. Lett. **211**, 147 (1993), **227**, 656 (1994).
[14] M. A. Buntine, D. W. Chandler, and C. C. Hayden, J. Chem. Phys. **102**, 2718 (1995).
[15] M. A. Buntine, D. W. Chandler, and C. C. Hayden, J. Chem. Phys. **97**, 707 (1992).
[16] T. J. Butenhoff and E. A. Rohlfing, J. Chem. Phys. **97**, 1595 (1992).
[17] S. Williams, J. D. Tobiason, J. R. Dunlop, and E. A. Rohlfing, J. Chem. Phys. **102**, 8342 (1995).
[18] W.-C. Hung, M.-L. Huang, Y.-C. Lee, and Y.-P. Lee, J. Chem. Phys. **103**, 9941 (1995).
[19] H. J. Eichler, P. Gunter, and D. W. Pohl, *Laser-Induced Dynamic Gratings* (Springer, Berlin, 1986).
[20] T. J. Butenhoff and E. A. Rohlfing, J. Chem. Phys. **98**, 5460 (1993), J. R. Dunlop and E. A. Rohlfing, *ibid*. **100**, 856 (1994).
[21] T. J. Butenhoff and E. A. Rohlfing, J. Chem. Phys. **98**, 5469 (1993).
[22] M. D. Wheeler, I. R. Lambert, and M. N. R. Ashfold, Chem. Phys. Lett. **229**, 285 (1994).
[23] T. Ebata, A. Okazaki, Y. Inokuchi, and N. Mikami, J. Mol. Struct. **352/353**, 533 (1995).
[24] G. Hall and B. J. Whitaker, J. Chem. Soc. Faraday Trans. **90**, 1 (1994).
[25] S. Williams, R. N. Zare, and L. A. Rahn, J. Chem. Phys. **101**, 1072 (1994).
[26] S. A. J. Druet and J.-P. E. Taran, Prog. Quantum Electron. **7**, 1 (1981).
[27] Y. Prior, IEEE J. Quantum Electron. **QE-20**, 37 (1984).
[28] T. K. Yee and T. K. Gustafson, Phys. Rev. A **18**, 1597 (1978).
[29] R. Trebino, Phys. Rev. A **38**, 2921 (1988).
[30] R. N. Zare, *Angular Momentum* (Wiley, New York, 1988).
[31] B. Attal-Trétout, P. Monot, and K. Muller-Dethlefs, Mol. Phys. **73**, 1257 (1991), B. Attal-Trétout and K. Muller-Dethlefs, Ber Bunsenges. Phys. Chem. **89**, 318 (1985).
[32] I. Aben, W. Ubachs, G. Van Der Zwan, and W. Hogervorst, Mol. Phys. **76**, 591 (1992).
[33] P. N. Butcher and D. Cotter, *The Elements of Nonlinear Optics* (Cambridge University Press, Cambridge, 1990).
[34] A. Omont, Prog. Quantum Electron. **5**, 69 (1977).
[35] S. Williams, L. A. Rahn, and R. N. Zare, J. Chem. Phys. **104**, 3947 (1996).
[36] R. C. Hiborn, Am. J. Phys. **50**, 982 (1982).
[37] M. Ducloy and D. Bloch, Phys. Rev. A **30**, 3107 (1984).
[38] K. Blum, *Density Matrix Theory and Applications* (Plenum, New York, 1981).
[39] P. R. Berman, D. G. Steel, G. Khitrova, and J. Liu, Phys. Rev. A **38**, 252 (1988).
[40] U. Fano and J. H. Macek, Rev. Mod. Phys. **45**, 553 (1973).
[41] C. H. Greene and R. N. Zare, J. Chem. Phys. **78**, 6741 (1983).
[42] A. J. Orr-Ewing and R. N. Zare, in *The Chemical Dynamics and Kinetics of Small Radicals*, edited by K. Liu and A. Wagner, Advanced Series in Physical Chemistry, edited by C.-Y. Ng (World Scientific, Singapore, 1995).
[43] E. Freidman-Hill, L. A. Rahn, and R. L. Farrow, J. Chem. Phys. **100**, 4065 (1993).
[44] L. Lehr, M. Motzkus, K. L. Kompa, and P. Hering, J. Chem. Phys. **104**, 9698 (1996).
[45] R. Altkorn and R. N. Zare, Annu. Rev. Phys. Chem. **35**, 265 (1984).
[46] A. Dreizler, T. Dreier, and J. Wolfrum, Chem. Phys. Lett. **233**, 525 (1995).
[47] D. E. Govoni, J. A. Booze, A. Sinha, and F. F. Crim, Chem. Phys. Lett. **216**, 525 (1993).
[48] J. T. Fourkas, R. Trebino, and M. D. Fayer, J. Chem. Phys. **97**, 69 (1992).
[49] J. T. Fourkas, R. Trebino, and M. D. Fayer, J. Chem. Phys. **97**, 78 (1992).
[50] J. A. Nunes, W. G. Tong, D. W. Chandler, and L. A. Rahn, Sandia Report No. SAND95-8221 (1995); D. W. Neyer, L. A. Rahn, D. W. Chandler, J. A. Nunes, and W. G. Tong (unpublished).